Monte Carlo Simulation of X-ray Transport

John Meneghini[a)]

Department of Physics, Saint Vincent College, Latrobe, PA 15650

[a)]Corresponding author: john.meneghini@stvincent.edu

Abstract. An article usually includes an abstract, a concise summary of the work covered at length in the main body of the article. It is used for secondary publications and for information retrieval purposes.

INTRODUCTION

Computed Tomography (CT) imaging is a critical diagnostic tool used by medical professionals to diagnose various illnesses and injuries. While the use of CT imaging is essential to provide immediate, life-saving results, it is critical to recognize and assess the dangers associated with ionizing radiation. In particular, ionizing radiation has the ability to damage DNA and increase the risk of cancer in patients. While the risk is small, it is cumulative, so it is important for physicians to track a patient's radiation exposure overtime [1]. To track said exposure, we must first be able to quantify and determine the dosage of radiation a patient receives during an imaging test. Typically, this exposure is measured using absorbed dose and air kerma at the skin layer, which both have units of grays (joule/kg), making it directly related to the energy deposited/incident by photons and their secondary particles. Often, these values are estimated based on the properties/settings of the x-ray source and the specific procedure being performed. However, the most accurate technique is the use of Monte Carlo (MC) methods to simulate the propagation of photons through a computational phantom [2].

In the MC technique, the 3D space encompassing the phantom and the radiation source is represented as a computational domain. Within this domain, individual photon interactions are stochastically simulated, accounting for each interaction event as photons navigate the phantom. This complexity in simulation offers unparalleled precision, capturing even the most subtle nuances of radiation behavior in biological media. Additionally, the MC method can simulate various tissue types, densities, and configurations, making it incredibly versatile and adaptable to varying imaging tests. Furthermore, advancements in computational power and algorithms have expedited the MC simulations, rendering them more accessible and feasible for routine clinical applications [3].

In this paper, the newly developed open source MC photon transport code system MIDSX is presented and validated. While many existing MC transport code systems have shown reliability in dosimetry applications [3, 4], many of these systems are tailored for general particle transport. While the capabilities of these code systems are far beyond that of MIDSX, the developmental focus on x-ray transport has reduced the complexity from an implementation point of view. In turn, allowing users to easily design and run simulations specifically relating to x-ray transport in the medical imaging energy range. The subsequent sections will delve into the theory of MIDSX, its methodology, and comparative analysis with other established systems.

TRANSPORT THEORY

In order to represent the computational domain discretely, space is broken up into a grid of voxels (a pixel with volume), with each voxel being assigned a particular material ID depending on the geometries and compounds/elements in the domain. Within our discrete space, given a photon position $\vec{r}$, the corresponding voxel in which the photon resides can be calculated. Therefore, all possible $\vec{r}$'s can be associated with a particular material M in the domain.

A photon's position in space after taking the n-th step in the domain, $\vec{r}_n$, is represented by the following parametric ray equation:

$$\vec{r}_n = \vec{r}_{n-1} + \hat{d}t_n, \tag{1}$$

where $\vec{r}_{n-1}$ is the initial position before the n-th step, $\hat{d}$ is a unit vector in the direction of the step, and t_n is the length of the n-th step.

In order to randomly sample t_n in a homogenous domain, we utilize the following probability density function (PDF) $p(t)$ of the distance traveled t by a photon of energy E through material M before interacting:

$$p(t) = n\sigma \exp[-t(n\sigma)], \tag{2}$$

where n is the number density of M and $\sigma = \sigma(E, M)$ is the microscopic cross-section of M at E.

Using the inversion method for sampling a PDF on Eq 2, it follows that random values of the free path t can be generated with the following equation:

$$t = -\frac{1}{n\sigma} \ln \gamma, \tag{3}$$

where γ is a uniformly distributed random number in the interval $[0, 1]$. This value of t is sampled for each step and is used as t_n in Eq 1 to determine the length of the n-th step.

For further reading on the theory presented in this section, see [5].

SURFACE AND DELTA-TRACKING

If, after taking a step, the photon lands in a voxel with a different material (an inhomogeneous domain), then the corresponding free path for the new material must be accounted for. One method, called surface-tracking, requires photons to be stopped at voxel boundaries and intersections with surrounding voxels to be calculated, which can be computationally intensive for materials that have a large average free path.

Alternatively, the delta-tracking algorithm offers a solution by sampling the maximum cross-section σ_{max} in the computational domain. This, in turn, brings down the average free path to the minimum in the domain. To account for this decrease in free path, the algorithm introduces delta interactions as an alternative to real interactions, resulting in no change to the energy or direction. The probability of delta interaction P_δ is given by the following equation:

$$P_\delta = \frac{\sigma_{max}(E) - \sigma(E, M)}{\sigma_{max}(E)}, \tag{4}$$

where E is the energy of the photon undergoing the step. Note that when the photon lands in the material corresponding to the maximum cross-section, $\sigma(E, M) = \sigma_{max}$ and $P_\delta = 0$. On the contrary, if the photon landed in air and the domain's maximum cross-section corresponded to lead, then $\sigma(E, M) << \sigma_{max}$, making $P_\sigma \approx 1$.

Overall, delta-tracking is significantly more computationally efficient for domains with similar cross-sections and can be shown to yield equivalent results to surface-tracking.

For more details on these algorithms, see [5].

PHOTON INTERACTIONS

If a delta interaction does not occur, then a real interaction is sampled. Therefore, the probability of a real interaction P_r is directly related to P_δ by

$$P_r = 1 - P_\delta, \tag{5}$$

where P_δ is given by Eq 4.

If a real interaction occurs in material M, then the probability of interaction i occurring is $P_i = \frac{\sigma_i(E,M)}{\sigma(E,M)}$ where σ_i is the cross-section of interaction i. If there are N possible interactions for a particular E and M, then $\sigma(E, M)$ is calculated as so

$$\sigma(E, M) = \sum_{i=1}^{N} \sigma_i(E, M). \tag{6}$$

For x-rays, there are three possible photon interactions: photoelectric effect, coherent scattering, and incoherent scatering. For the photoelectric effect, the photon is terminated and all energy is deposited at the location of interaction. In general purpose particle transport code systems, when a photoelectric interaction occurs, a photon of energy E is absorbed by an electron in subshell i, causing the electron to leave the atom with energy $E_e = E - U_i$, where U_i is the binding energy of the ith subshell. In addition, photons are emitted due to atomic relaxations. For photon energies in the medical imaging range (30 - 120 keV), the energy of the released electrons does not allow for significant traversal through typical biological media. This limited traversal results in a localized dose distribution, in turn, validating the model used by MIDSX.

For coherent and incoherent scattering, the methodology of [6] was adapted for use in MIDSX, neglecting Doppler energy broadening and the production of secondary particles.

IMPLEMENTATION

To simulate x-ray transport in MIDSX, the domain's geometry is represented using a 3D voxel array with each voxel assigned a material ID. Geometries are defined by NIFTI files [7] and incorporated into a custom .domain file. The code employs `VoxelGrid` objects which are contained within `ComputationalDomain` objects.

Materials are defined in an SQLite database [8] containing elemental data from [9] and [10], and interaction data from the EPDL database [11]. The `InteractionData` object initializes this material data with various interpolation methods, including linear and spline interpolation.

The `PhotonSource` object, initialized with `SourceGeometry`, `Directionality`, and `EnergySpectrum`, determines the photon's initial attributes. MIDSX provides measurement triggers through surface and volume tallies. The geometries of these tallies correspond to regions of interest (ROI) and volumes of interest (VOI), respectively. Users can specify desired tally quantities via the `Quantity` and `QuantityContainer` objects, with post-simulation derived quantities like air kerma computed using the `DerivedQuantity` object.

For more details on the methodology used in MIDSX, see [12].

RESULTS

In order to validate the accuracy of MIDSX, validation simulations were performed and compared to reference data obtained by American Association of Physicists in Medicine Task Group Report 195 (TG-195) [13]. The simulations performed from TG-195 were Case 1: "Half Value Layer", Case 2: "Radiography and Body Tomosynthesis", and Case 5: "CT with a Voxelized Solid". For Case 1, the primary air kerma was measured on a far away, circular region of interest (ROI) with a cone beam collimated such that all primary particles would be incident upon the ROI. The primary air kerma was measured with the domain filled only with air, and then compared to the measured air kerma with an Al filter of specified thickness placed between the source and ROI. By setting this thickness to correspond the half value layer (HVL) and quarter value layer (QVL) for a particular spectrum, one is able to validate the material attenuation properties of an MC code system. The ratios of the primary half value layer (HVL) and air kermas to the primary background air kermas is represented by R_1 and R_2, respectively. The simulation was performed for the monoenergetic energies 30 keV and 100 keV, along with the polyenergetic spectrums of 30 kVp and 100 kVp, which were provided by TG-195. MIDSX's results for Case 1 agree to within 0.32% of the mean results published by TG-195, and only the simulation results of 100 keV x-ray spectrum fell withing the range of the published results for both the HVL and QVL simulations. The results of Case 1 are presented in Fig 1.

For Case 2, a full-field and pencil beam x-ray source were directed towards a rectangular tissue phantom at $0°$ and $15°$ with respect to the z-axis. Directly behind and inside the phantom, a grid of square ROIs and cube VOIs were placed, respectively. The simulation was performed for the TG-195 provided polyenergetic spectrum of 120 kVp and its mean energy of 56.4 keV. For the $0°$ full-field ROI measurements not shown in this paper due page constraints, a $< 3\%$ mean percent error (MPE) is seen for MIDSX's results to each ROI simulation. Furthermore, for the $0°$ pencil-beam ROI measurements shown in Fig 3, a $< 2.1\%$ MPE is observed for each ROI simulation expect for the case of a single incoherent scatter. In this particular case, MIDSX's results for ROI 4 and 5 are significantly lower, with the MPE reaching 10% for ROI 5. In the full-field VOI energy deposition measurements depicted in Fig 2, the disagreement between code systems is minimal with an MPE of less than 0.1% for the $0°$ source. Conversely, for the MIDSX results at $15°$, the MPE reaches approximately 0.5%.

For Case 5, a fan beam was collimated to the center of a voxelized human torso phantom provided by TG-195. In order to replicate a CT image, the simulation was repeated for several angles along a circle surrounding the phantom. The simulation was performed with Case 2's 120 kVp energy spectrum, and energy deposition was measured in the different materials/organs composing the phantom. Almost all of MIDSX's results for the 0° source presented in Fig 4 are systematically lower than the mean of the reference code systems, with MPE's ranging from 1.1% to 6.3%. This pattern is disrupted by the thyroid, which is larger than the mean by 2.9%. In order to quantify the cumulative error, the root mean square percent error (RMSPE) was calculated using each organ result, which resulted in the RMSPE for MIDSX being 5%.

As with the reference code systems, each simulation was run until an error of up to 1% was reached. For MIDSX, this error represented the standard deviation.
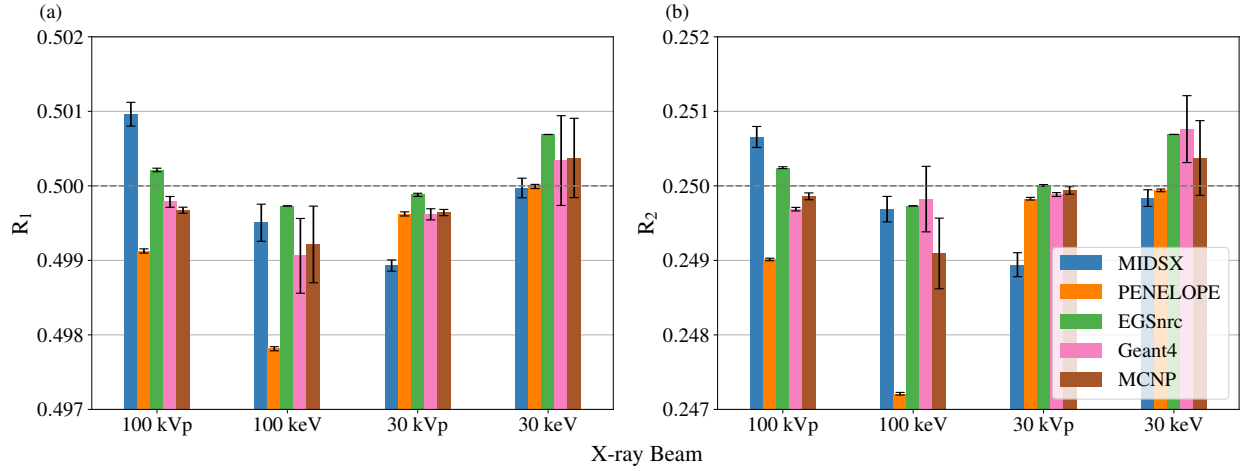

FIGURE 1: Results for the (a) HVL and (b) QVL simulations as described by Case 1. The ratios of the primary HVL and QVL air kermas to the primary background air kermas is represented by R_1 and R_2, respectively. The simulation was performed for the monoenergetic energies 30 keV and 100 keV, along with the polyenergetic spectrums of 30 kVp and 100 kVp, which were provided by TG-195.
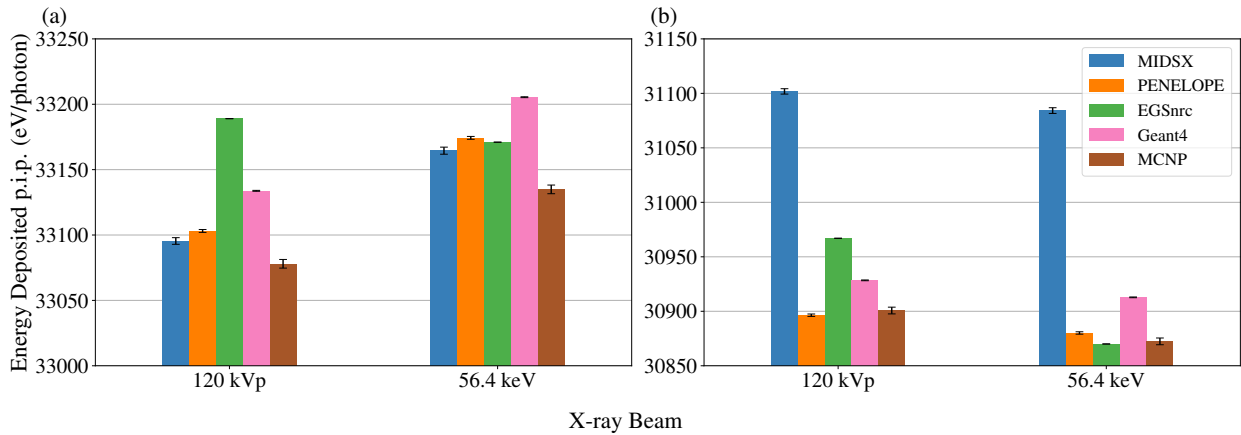

FIGURE 2: The energy deposited per initial photon (eV/photon) in the simulated tissue for the full-field simulation as described by Case 2. The simulation was performed at 56.4 keV and 120 kVp at both (a) 0° and (b) 15°, with the 120 kVp spectrum provided by TG-195.

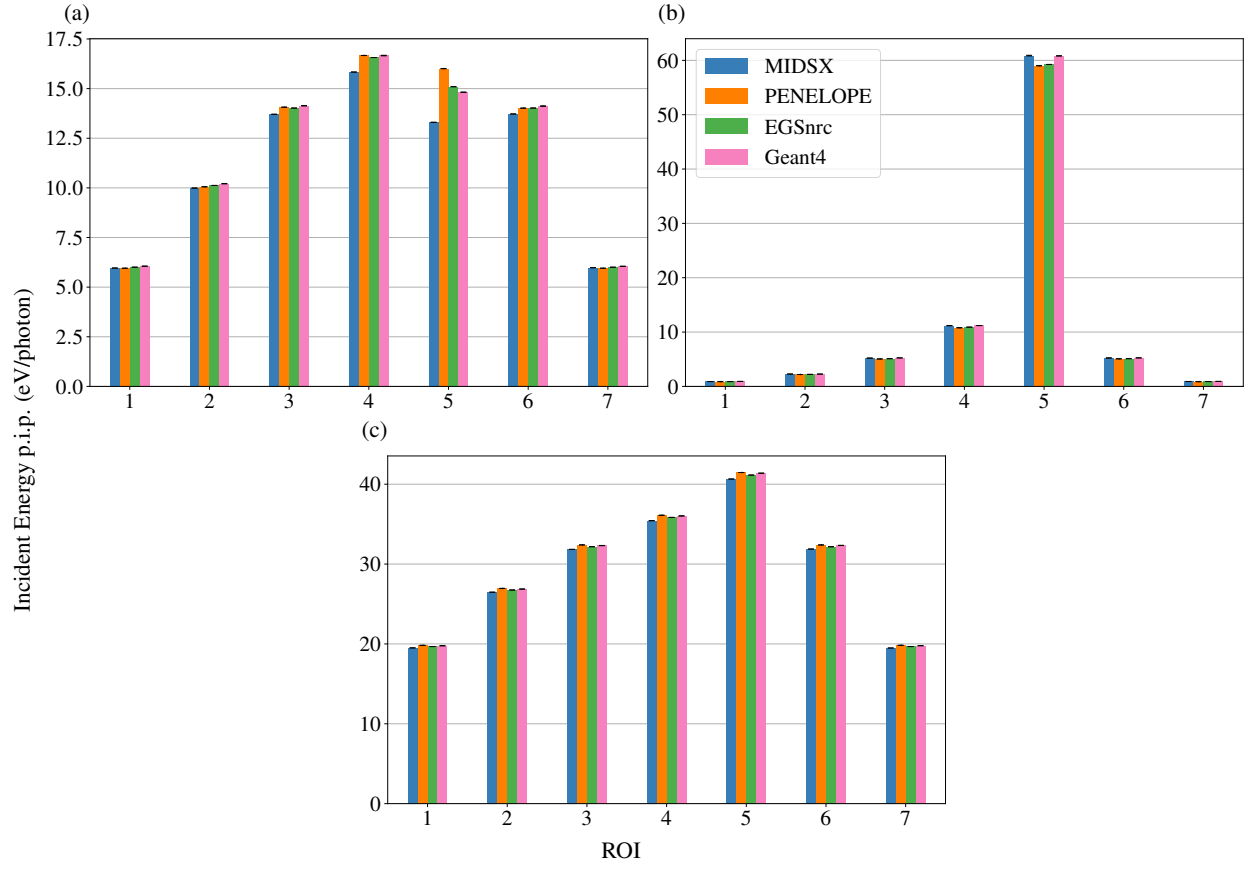FIGURE 3: The energy per initial photon (eV/photon) of photons incident upon each region of interest (ROI) for the 0°, pencil beam, 56.4 keV simulation as described by Case 2. The incident energy was determined separately for photons that underwent (a) a single incoherent scatter, (b) a single coherent scatter, (c) and multiple scatters.
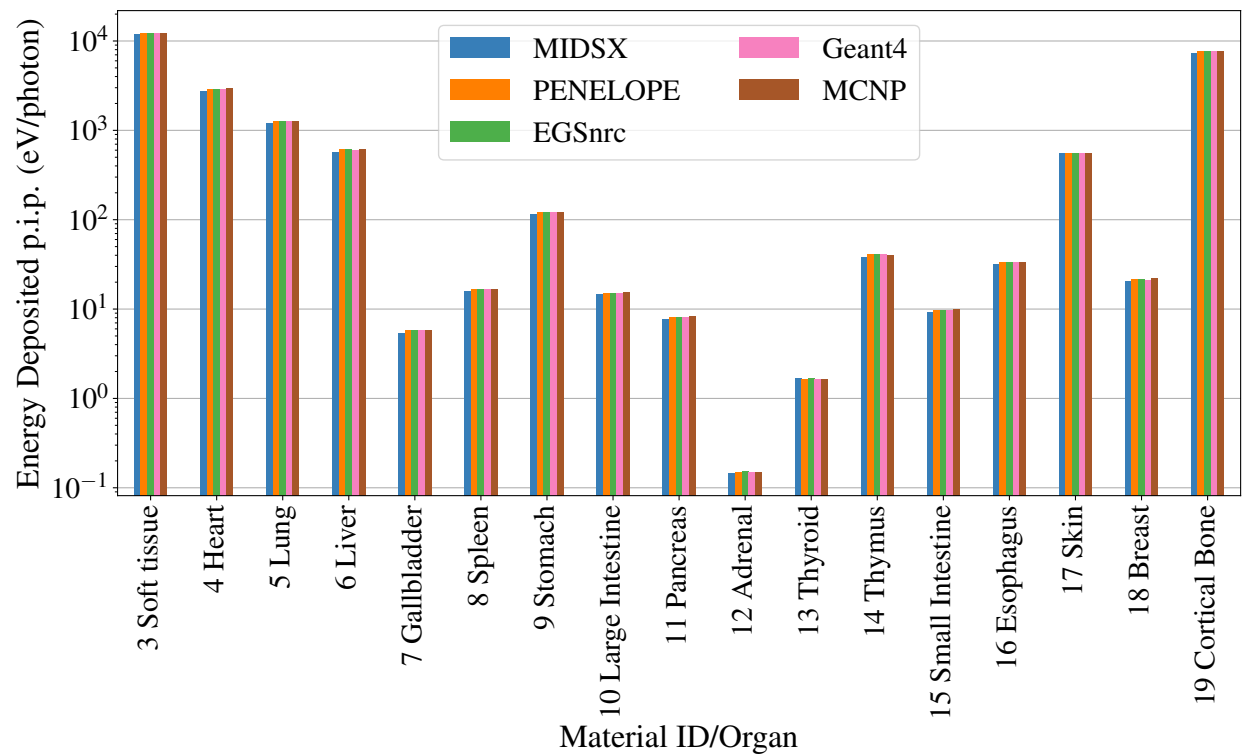
FIGURE 4: The energy deposited per initial photon (eV/photon) in the material IDs for the 0°, 120 kVp simulation as described by Case 5.

DISCUSSION

Overall, MIDSX shows relative agreement with the PENELOPE, EGSnrc, Geant4, and MCNP results provided by TG-195 for the three examined cases. For the HVL layer simulation described by Case 1, statistical agreement is seen with all code systems except for PENELOPE for the HVL and QVL 100 keV simulation. In addition, for the 30 keV simulation, statistical agreement is seen with PENELOPE, Geant4, and MCNP for HVL, along with PENELOPE and MCNP for QVL. Note that while no statistical agreement is observed for the other energies/thicknesses, all MIDSX results are within 0.32% of the mean of the reference code systems.

For Case 2, agreement is rather varied. For the full-field ROI measurements not shown in this paper due page constraints, very little statistical agreement is seen between the code systems; however, a $< 3\%$ mean percent error (MPE) is seen for MIDSX's results to each ROI simulation. Furthermore, for the pencil-beam ROI measurements shown in Fig 3, statistical agreement is not readily observed, but a $< 2.1\%$ MPE is observed for each ROI simulation expect for the case of a single incoherent scatter. In this particular case, MIDSX's results for ROI 4 and 5 are significantly lower, with the MPE reaching 10% for ROI 5. This discrepancy is likely a result of an error in the rejection sampling algorithm employed by MIDSX. While this algorithm shows agreement for the full-field ROI 5, the geometry of the ROI, combined with the pencil beam, results in only narrow angle scatters hitting the ROI. Since the scattering angle distribution of incoherent scattering at the medical imaging energy range contains a vertical asymptote approaching 0 at $\theta = 0°$, there is likely some form of numerical instability presenting itself in the algorithm that needs to be analyzed.

In the full-field tissue deposition measurements depicted in Fig 2, we do not observe statistical agreement. However, for the $0°$ case, the disagreement between code systems is minimal with an MPE of less than 0.1% for MIDSX. Conversely, for the MIDSX results at $15°$, the MPE reaches approximately 0.5%. Despite extensive investigations into this pronounced discrepancy, a solution remains elusive.

For Case 5, almost all of MIDSX's results are marginally lower than the mean of the reference code systems, with MPE's ranging from 1.1% to 6.3%. This pattern is disrupted by the thyroid, which is larger than the mean by 2.9%. In order to quantify the cumulative error, the root mean square percent error (RMSPE) was calculated using each organ result, which resulted in the RMSPE for MIDSX being 5%. In addition, with all other code systems typically having an MPE less than 1%, except for MCNP which reaches an MPE of 2.2% for the breast, there appears to a systematic error with the MIDSX code system with regard to the CT simulation. One common error reported by TG-195 is the incorrect orientation of the voxelized phantom in the computational domain. On top of checking the scenes geometry and the .comp file, the orientation was verified by taking the RMSPE of the MIDSX data with respect to the results of each simulated angle reported by TG-195. As expected, the RMSPE with respect the $0°$ was the minimum, further solidifying the belief that the phantom's orientation during the CT simulation is accurate.

However, despite the orientation being verified, the consistent deviation of MIDSX energy deposition results for both Case 2 and 5 raises concerns. This suggests that there may be other underlying issues or intricacies in the MIDSX system that need further investigation. Potential factors could include the software's handling of certain physics processes, voxel resolution, or computational approximations. It's imperative for future research to delve deeper into these aspects to pinpoint and rectify the source of the systematic errors observed in the MIDSX results.

ACKNOWLEDGMENTS

REFERENCES

1. Michael S Lauer. Elements of danger—the case of medical imaging. *Minnesota Medicine*, 92(12):40, 2009.

2. Jerrold T. Bushberg, J. Anthony Seibert, Edwin M. Leidholdt, Jr., and John M. Boone. *X-ray Dosimetry in Projection Imaging and Computed Tomography*, chapter 11, pages 375–401. Wolters Kluwer Health/Lippincott Williams & Wilkins, 3rd edition, 2012.

3. David Fernández Bosman, Victor García Balcaza, Clara Delgado, Sara Principi, Maria Amor Duch, and Mercè Ginjaume. Validation of the MC-GPU Monte Carlo code against the PENELOPE/penEasy code system and benchmarking against experimental conditions for typical radiation qualities and setups in interventional radiology and cardiology. *Physica Medica*, 82:64–71, February 2021. ISSN 11201797. doi: 10.1016/j.ejmp.2021.01.075. URL https://linkinghub.elsevier.com/retrieve/pii/S1120179721000788.

4. J.-F. Carrier, L. Archambault, L. Beaulieu, and R. Roy. Validation of geant4, an object-oriented monte carlo toolkit, for simulations in medical physics. *Medical Physics*, 31(3):484–492, 2004. doi:https://doi.org/10.1118/1.1644532. URL `https://aapm.onlinelibrary.wiley.com/doi/abs/10.1118/1.1644532`.

5. Oleg N. Vassiliev. *Monte Carlo Methods for Radiation Transport*. Biological and Medical Physics, Biomedical Engineering. Springer International Publishing, Cham, 2017. ISBN 978-3-319-44140-5 978-3-319-44141-2. doi:10.1007/978-3-319-44141-2.

6. Amanda L Lund and Paul K Romano. Implementation and validation of photon transport in openmc. Technical report, Argonne National Lab.(ANL), Argonne, IL (United States), 2018.

7. R.W. Cox, John Ashburner, Hester Breman, Kate Fissell, C. Haselgrove, C.J. Holmes, J.L. Lancaster, D.E. Rex, S.M. Smith, J.B. Woodward, and Stephen Strother. A (sort of) new image data format standard: Nifti-1. volume 22, 01 2004.

8. Richard D Hipp. SQLite, 2020. URL `https://www.sqlite.org/index.html`.

9. Paul Kienzle. periodictable - a python library for periodic table of the elements, May 2022. URL `https://github.com/pkienzle/periodictable`.

10. Łukasz Mentel. mendeleev - a python package with properties of chemical elements, ions, isotopes and methods to manipulate and visualize periodic table., March 2021. URL `https://github.com/lmmentel/mendeleev`.

11. Dermott E Cullen. A Survey of Photon Cross Section Data for use in EPICS2017. November 2017.

12. John Meneghini. MIDSX, 2023. URL `https://github.com/jmeneghini/MIDSX`.

13. Ioannis Sechopoulos, Elsayed S. M. Ali, Andreu Badal, Aldo Badano, John M. Boone, Iacovos S. Kyprianou, Ernesto Mainegra-Hing, Kyle L. McMillan, Michael F. McNitt-Gray, D. W. O. Rogers, Ehsan Samei, and Adam C. Turner. Monte Carlo reference data sets for imaging research: Executive summary of the report of AAPM Research Committee Task Group 195. *Medical Physics*, 42(10):5679–5691, October 2015. ISSN 0094-2405, 2473-4209. doi:10.1118/1.4928676. URL `https://onlinelibrary.wiley.com/doi/10.1118/1.4928676`.